JACS Au
AN OPEN ACCESS JOURNAL OF THE AMERICAN CHEMICAL SOCIETY

pubs.acs.org/jacsau
Article

Bioinspired Binickel Catalyst for Carbon Dioxide Reduction: The Importance of Metal−ligand Cooperation

Yao Xiao, Fei Xie, Hong-Tao Zhang, and Ming-Tian Zhang*

Cite This: JACS Au 2024, 4, 1207−1218

Read Online

ACCESS | Metrics & More | Article Recommendations | Supporting Information

ABSTRACT: Catalyst design for the efficient CO_2 reduction reaction (CO_2RR) remains a crucial challenge for the conversion of CO_2 to fuels. Natural Ni−Fe carbon monoxide dehydrogenase (NiFe-CODH) achieves reversible conversion of CO_2 and CO at nearly thermodynamic equilibrium potential, which provides a template for developing CO_2RR catalysts. However, compared with the natural enzyme, most biomimetic synthetic Ni−Fe complexes exhibit negligible CO_2RR catalytic activities, which emphasizes the significance of effective bimetallic cooperation for CO_2 activation. Enlightened by bimetallic synergy, we herein report a dinickel complex, $Ni^{II}Ni^{II}(bphpp)(AcO)_2$ (where **NiNi(bphpp)** is derived from H_2bphpp = 2,9-bis(5-*tert*-butyl-2-hydroxy-3-pyridylphenyl)-1,10-phenanthroline) for electrocatalytic reduction of CO_2 to CO, which exhibits a remarkable reactivity approximately 5 times higher than that of the mononuclear Ni catalyst. Electrochemical and computational studies have revealed that the redox-active phenanthroline moiety effectively modulates the electron injection and transfer akin to the $[Fe_3S_4]$ cluster in NiFe-CODH, and the secondary Ni site facilitates the C−O bond activation and cleavage through electron mediation and Lewis acid characteristics. Our work underscores the significant role of bimetallic cooperation in CO_2 reduction catalysis and provides valuable guidance for the rational design of CO_2RR catalysts.

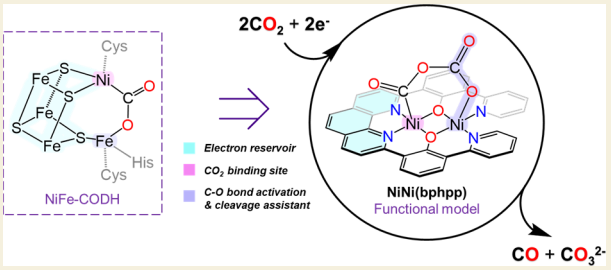

KEYWORDS: *CO_2 reduction, binickel catalyst, homogeneous catalysis, C−O bond cleavage, bimetallic cooperative catalysis, redox-active ligand*

INTRODUCTION

The reduction of CO_2 to CO is a promising strategy for utilizing CO_2 as a renewable C_1 feedstock and establishing an artificial carbon cycle.[1−5] Despite numerous studies on transition-metal-based CO_2RR molecular catalysts, including those based on Re,[6−10] Rh,[11−13] Ru,[14−23] Fe,[24−37] Ni,[38−44] Co,[45−55] Mn,[56−63] Cr,[64,65] and so forth,[66−70] challenge persists in bridging the gap between current advances and practical applications, and thus the design of efficient molecular catalysts remains a significant challenge.[71−74] In nature, carbon monoxide dehydrogenase (CODH) plays a pivotal role in biological carbon fixation processes. This enzyme proceeds the binding of CO and CO_2 to its Ni−Fe bimetallic active center, followed by electron transfer to the substrate, enabling the reversible conversion.[75−80] NiFe-CODH exemplifies the importance of bimetallic synergy in CO_2 reduction catalysis: it activates CO_2 at only −0.6 V versus standard hydrogen electrode (SHE) through the Ni site, with a $[Fe_3S_4]$ cluster serving as an electron mediator. Upon protonation of Ni-CO_2, the Fe site promotes the hydroxide elimination as a Lewis acid, thereby catalyzing the conversion of CO_2 to CO (Scheme 1a).[81−83] This mechanism indicates that dinuclear metal complexes are promising candidates for CO_2 reduction catalysis, as evidenced in several bimetallic catalytic systems.[84−99]

Although structure similarities in bimetallic catalytic intermediates, such as $Pd(\mu_2\text{-}\eta^2\text{-}CO_2)Pd$[85,87] and $Co(\mu_2\text{-}\eta^2\text{-}C,O\text{:}\eta^1\text{-}O)Co$,[91] suggest that the structure feature of NiFe-CODH could inform the development of artificial bimetallic catalysts, the synthesized Ni−Fe clusters and macrocyclic Ni−Fe complexes with closely positioned metals have yet to demonstrate the catalytic activity for CO_2 reduction.[100−109] These findings underscore that simply combining two metals does not replicate the catalytic function of NiFe-CODH and also highlight the necessity of integrating CO_2 complexation, effective electron transfer, stabilization of intermediates, and an appropriate geometric arrangement of the catalyst to facilitate C−O bond cleavage and CO release. Meanwhile, two primary mechanisms of bimetallic cooperative CO_2 activation have been proposed: $M_1(\mu_2\text{-}\eta^2\text{-}CO_2)M_2$ and $M_1(\mu_2\text{−}C(O)OC(O)\text{-}$

Received: January 10, 2024
Revised: February 17, 2024
Accepted: February 21, 2024
Published: March 11, 2024

Scheme 1. (a) Structure of the NiFe-CODH Active Site; (b) Proposed Two Modes of Bimetallic CO_2 Activation; (c) CO_2 Reduction by the Designed Dinickel Catalyst in This Work

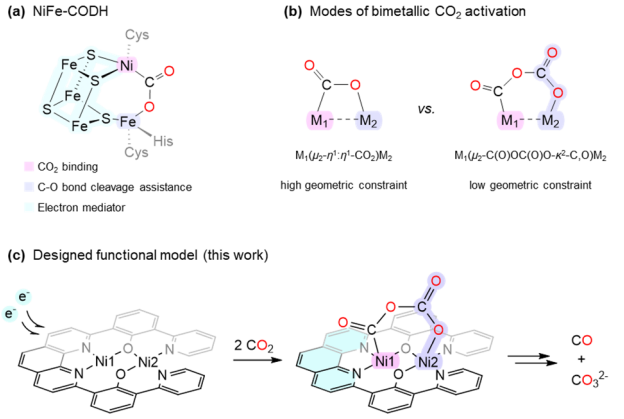

O−κ^2-*C,O*)M_2 (Scheme 1b).[85,91,95,110,111] For the former, maintaining a close intermetallic distance (<3.0 Å) is crucial,[108] which imposes a higher geometric constraint. Conversely, the latter mechanism can accommodate various geometries, potentially allowing for closer positioning and enhanced interaction between the metal sites.

Herein, as depicted in Scheme 1c, we designed a well-structured dinickel complex with a nearly planar geometry. Taking inspiration from the $[Fe_3S_4]$ cluster in NiFe-CODH, we employed a redox-active phenanthroline ligand[112] as an electron reservoir. This design facilitates electron transfer and enhances CO_2 binding at the coordinated Ni1 site. Furthermore, the secondary Ni2 site, which possesses a distinct coordination environment, aids in the activation and cleavage of the C−O bond. This is achieved through a [Ni(μ_2−C(O)OC(O)O−κ^2-*C,O*)Ni] six-membered ring intermediate, which mitigates the geometry constraints associated with bimetallic centers. The binuclear [$Ni^{II}Ni^{II}$(bphpp)-$(AcO)_2$] complex (**NiNi(bphpp)**) demonstrates high reactivity in the catalytic reduction of CO_2 to CO and promotes the generation of CO_3^{2-} through ligand reduction and bimetallic synergy. This work holds the potential to make a substantial contribution to the development of novel strategies for CO_2 capture and utilization.

RESULTS AND DISCUSSION

Synthesis and Characterization of NiNi(bphpp) and Ni(hbpp)

H_2bphpp (2,9-bis(5-*tert*-butyl-2-hydroxy-3-pyridylphenyl)-1,10-phenanthroline) and H_2hbpp (2,9-bis(5-*tert*-butyl-2-hydroxyphenyl)-1,10-phenanthroline) are synthesized by the modified procedures[113] and used as the dinuclear and mononuclear ligands, respectively (Scheme S1, Figures S1−S15). The dinickel complex **NiNi(bphpp)** and mononickel complex [Ni^{II}(hbpp)] (**Ni(hbpp)**) are prepared by mixing the corresponding ligand with 2 equiv or 1 equiv $Ni(AcO)_2{\cdot}4H_2O$, respectively, which are detailed in the Supporting Information (SI). The X-ray crystal structure of **NiNi(bphpp)** shows that the two Ni^{II} ions are both in an octahedral geometry configuration, which are bridged by two phenolic O atoms and connected by two acetates located above and below the ligand plane (Figures 1a and S16). The distance between the

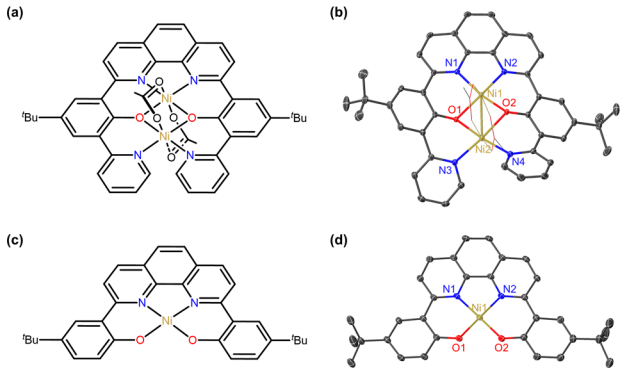

Figure 1. Schematic structures and X-ray crystal structures of **NiNi(bphpp)** (a), (b) and **Ni(hbpp)** (c), (d), respectively. Ellipsoids are shown at 80% probability of atoms and 60% probability of bonds. Two acetate anions are drawn in wireframe style; the hydrogen atoms and solvent molecules are omitted for clarity.

two Ni^{II} sites is 2.70 Å, which is similar to the distance of 2.8 Å between Ni and Fe in CODH,[81,83,108] indicating a suitable geometric structure required for CO_2 activation. In contrast, the X-ray crystal structure of **Ni(hbpp)** shows that the Ni^{II} ion has a square-planar configuration (Figures 1b and S17), consistent with low-spin Ni^{II} ($S = 0$) characterized by ^{1}H NMR (Figure S18). **NiNi(bphpp)** and **Ni(hbpp)** were also characterized by high-resolution mass spectrometry (HRMS) in methanol, which showed the molecular cation peak at m/z 372.0763 ([$Ni^{II}Ni^{II}$(bphpp)]$^{2+}$, Figure S19) and m/z 555.1557 ([Ni^{II}(hbpp) + Na]$^+$, Figure S20), respectively. These results suggest that **NiNi(bphpp)** and **Ni(hbpp)** exist as di- and mononickel species in solution, respectively. In addition, the density functional theory (DFT) study showed that the dissociation energy of acetate in **NiNi(bphpp)** is 13.5 kcal/mol (Figure S41), indicating the consistency of the crystal structure with that in solution.

The electronic configuration of **NiNi(bphpp)** is further investigated. The Evans effective magnetic moment (μ_{eff}) was measured to be 4.16 μ_B at 290 K (Table S4, detailed in SI),[114,115] which is consistent with the spin multiplicity of S = 2. The magnetic properties of **NiNi(bphpp)** were obtained over the temperature range of 1.8−300 K by a superconducting quantum interference device (SQUID, Figure S21). The calculated effective magnetic moment, μ_{eff}, was 4.5 μ_B at the range 200−300 K, which is consistent with the measurement obtained using the Evans method, indicating a total spin state of S = 2. As the temperature decreases, the magnetic susceptibility increases, reaching a maximum of 5.3 μ_B at 10 K, which is close to the expected μ_{eff} for a two-spin-only S = 1 Ni^{II} system ($\mu_{eff.s.o} = 2.8 \times 2 = 5.6\ \mu_B$), suggesting the two Ni^{II} ions are weakly ferromagnetic coupled. These results agree well with the DFT calculation of the ground state electronic structure of **NiNi(bphpp)** that indicates a quintuple state (Figure S48). The μ_{eff} decreases to 4.0 μ_B at 1.8 K, which could be ascribed to the zero-field splitting (zfs) of the ground state. The two Ni^{II} ions of **NiNi(bphpp)** are assumed to be equivalent with the same zfs parameters D_1, rhombicity E/D, and electronic g-tensors. VT-VH magnetic susceptibility was collected at 1, 4, and 7 T (Figure S21). Global simulation of the VT-VH magnetic susceptibility and magnetization data, based on the spin-Hamiltonian (Section 1 of SI) of the low-lying electronic states, yielded an exchange coupling J = 7.4 cm^{-1}, and $D_1 = D_2 = -9.4\ cm^{-1}$ with strongly anisotropic g

https://doi.org/10.1021/jacsau.4c00047
JACS Au 2024, 4, 1207−1218

values of $g_x = g_y = 2.10$ and $g_z = 2.33$ for each Ni^{II} ion. The X-band EPR spectra of **NiNi(bphpp)** for orientations of the microwave field B_1 parallel and perpendicular to static field H were both obtained at 5 K in frozen DMF solution (Figure S22), and the valleys at $g = 12.6$ and $g = 9.9$ were observed, respectively. For this non-Kramers dinuclear Ni system, large D_1 values of each Ni^{II} ion were obtained from the magnetic data fitting and comparable to the exchange coupling, J, causing the $S = 2$ and $S = 1$ multiplets to mix,[116−118] and the zero-field absorption would origin from the energy levels with splitting in energy $\Delta \approx 0.3\ cm^{-1}$. Simulation of the parallel mode and perpendicular mode spectra gives $E/D \approx 0.12$ with $Dstrain = 0.1\ cm^{-1}$ and $Estrain = 0.05\ cm^{-1}$ for the broad lines.

Electrochemical Studies of NiNi(bphpp) and Ni(hbpp)

The redox behavior of **NiNi(bphpp)** was examined by cyclic voltammogram (CV) and differential pulse voltammetry (DPV) measurements in anhydrous degassed DMF. The CV and DPV of **NiNi(bphpp)** show four consecutive reduction waves at −1.68, − 1.80, − 2.14, and −2.44 V vs $Fc^{+/0}$ (Figures 2a and S25, all potentials below quoted vs $Fc^{+/0}$). The scan-rate-dependent CVs illustrate that the first wave is reversible with a peak-to-peak separation (ΔE_p) of 70 mV at a scan rate of 0.1 V/s (Figure S26), suggestive of a one-electron reduction process. The subsequent three waves are found to be irreversible (Figure S25). To elucidate the electrochemical processes associated with each reduction peak, a trizinc complex, $Zn_3(bphpp)(AcO)_4$, was synthesized (Figures S23 and S24). Its CV displayed two successive irreversible reduction waves at −1.86 and −1.98 V (Figure S27),[119] indicating that the initial two reduction peaks in the CV of **NiNi(bphpp)** are attributable to the reduction of the phenanthroline moiety. DFT studies were employed to further investigate the electrochemical processes. The one-electron reduction of **NiNi(bphpp)** (**1**) leads to the formation of the $Ni^{II}Ni^{II}(bphpp^{-\bullet})(AcO)_2$ species (**2**), which exhibits a spin population of 0.82 on the phenanthroline moiety, and the potential of this reduction process is calculated to be −1.65 V (eq 1, Figure S49). At the calculated potential of −1.69 V, $Ni^{II}Ni^{II}(bphpp^{-\bullet})(AcO)_2$ can accept an additional electron at the phenanthroline moiety to generate $Ni^{II}Ni^{II}(bphpp^{2-})(AcO)_2$ ($\mathbf{3}_{+2AcO}$, Figure S50). The two AcO^- ligands of $\mathbf{3}_{+2AcO}$ readily dissociate with a Gibbs free energy change of −11.3 kcal/mol, which is followed by charge redistribution, leading to the formation of $Ni^{I}Ni^{I}(bphpp)$ (**3**, eq 2). Moreover, even at a scan rate of 2.5 V/s, the second reduction wave remains irreversible, suggesting that the dissociation rate of the two AcO^- groups exceeds a certain threshold (Figure S28). Additionally, the reverse oxidation scan following the second reduction wave is tentatively ascribed to two-electron oxidation of the $Ni^{I}Ni^{I}(bphpp)$ species. Subsequently, the phenanthroline unit of $Ni^{I}Ni^{I}(bphpp)$ undergoes two successive one-electron reductions at −1.75 and −2.27 V, resulting in the generations of $Ni^{I}Ni^{I}(bphpp^{-\bullet})$ (**4**, eq 3, Figure S51) and $Ni^{I}Ni^{I}(bphpp^{2-})$ ($\mathbf{4}_{red}$, eq 4, Figure S52), respectively. These findings align with the observed experimental electrochemical behavior and highlight the role of the phenanthroline moiety as an electron reservoir. For **Ni(hbpp)**, the CV and DPV show two reduction peaks at −1.83 and −2.46 V, which are more negative than those observed for **NiNi(bphpp)** (Figures 2a and S29). The scan-rate-dependent CVs for **Ni(hbpp)** also indicate that the first wave is reversible, with a ΔE_p value of 66 mV at 0.1 V/s (Figure S30), consistent with a one-electron reduction. These reduction potentials are similar to those reported for (^{tbu}thbpy)FeCl by Machan et al.,[120] which are proposed to represent two consecutive one-electron reductions, leading to the formation of $Ni^{II}(hbpp^{-\bullet})$ and $Ni^{II}(hbpp^{2-})$, respectively. These findings are consistent with DFT results (see Figure S60). The CV comparisons demonstrate that both the phenanthroline moiety and the secondary Ni site in **NiNi(bphpp)** could help mitigate charge accumulation.

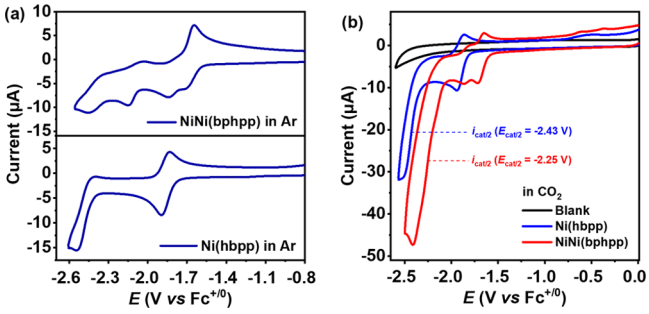

Figure 2. (a) CVs of 0.5 mM **NiNi(bphpp)** and 0.5 mM **Ni(hbpp)** under Ar atmosphere; (b) CVs of 0.5 mM **NiNi(bphpp)** (red line) and 0.5 mM **Ni(hbpp)** (blue line) under saturated CO_2 atmosphere, and CV under saturated CO_2 without catalyst (black line) using a glassy carbon electrode at 100 mV/s in 0.1 M $^nBu_4NPF_6$/DMF electrolyte.

$$Ni^{II}Ni^{II}(L)(AcO)_2 \xrightarrow{e^-} Ni^{II}Ni^{II}(L^{-\bullet})(AcO)_2 \quad \varphi_1 = -1.68\ V\ (Calc: -1.65\ V) \quad (1)$$

$$Ni^{II}Ni^{II}(L^{-\bullet})(AcO)_2 \xrightarrow[2\ AcO^-]{e^-} Ni^{I}Ni^{I}(L) \quad \varphi_2 = -1.80\ V\ (Calc: -1.69\ V) \quad (2)$$

$$Ni^{I}Ni^{I}(L) \xrightarrow{e^-} Ni^{I}Ni^{I}(L^{-\bullet}) \quad \varphi_3 = -2.14\ V\ (Calc: -1.75\ V) \quad (3)$$

$$Ni^{I}Ni^{I}(L^{-\bullet}) \xrightarrow{e^-} Ni^{I}Ni^{I}(L^{2-}) \quad \varphi_4 = -2.44\ V\ (Calc: -2.27\ V) \quad (4)$$

In CO_2-saturated anhydrous DMF solution (0.23 M[4]), the CV of **NiNi(bphpp)** shows a significant current enhancement, with a half peak potential ($E_{cat/2}$) of −2.25 V and peak potential at −2.40 V (Figure 2b).[121] The overpotential is determined to be 1.52 V concerning the estimated potential for the CO_2/CO couple in anhydrous DMF. this value is comparable to those reported for past catalytic systems in aprotic solutions.[60,95,122,123] In contrast, the $E_{cat/2}$ of **Ni(hbpp)** is ca. −2.43 V under the same condition (Figure 2b), where the overpotential is more negative by 0.18 V than that of the dinickel catalyst. This suggests that the introduction of a secondary Ni site decreases the overpotential for catalysis by facilitating charge accumulation. According to the CVs of **NiNi(bphpp)** under Ar and CO_2 atmosphere, the third irreversible reduction wave is attributed to the catalytic CO_2 reduction by the $Ni^{I}Ni^{I}(bphpp^{-\bullet})$ species. For **Ni(hbpp)**, the electrochemical properties indicate that the species formed after two-electron reduction, that is $Ni^{II}(hbpp^{2-})$ (Figure S60), is responsible for catalyzing CO_2 reduction.

To confirm the products of electrocatalytic CO_2 reduction, controlled potential electrolysis (CPE) of 0.5 mM **NiNi(bphpp)** at −2.20 V was carried out using a foamed graphite

https://doi.org/10.1021/jacsau.4c00047
JACS Au 2024, 4, 1207−1218

electrode (1.0 × 1.0 × 0.6 cm^3). The electrolysis current remained stable at an absolute value of approximately 2.8 mA, with a total charge consumption of 53.6 coulombs over 5 h (Figures 3a and S31). Gas chromatography (GC) and ion

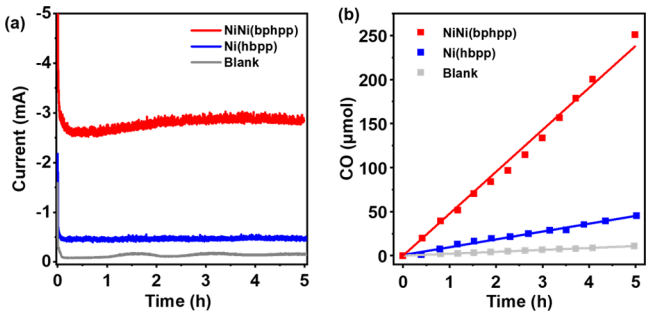

Figure 3. (a) CPE current curves of 0.5 mM **NiNi(bphpp)** (red line), 0.5 mM **Ni(hbpp)** (blue line) in anhydrous 0.1 M ^{n}Bu$_4$NPF$_6$/DMF, and blank solution (gray line) at −2.20 V; (b) CO production curves of 0.5 mM **NiNi(bphpp)** (red dot), 0.5 mM **Ni(hbpp)** (blue dot), and no catalyst (gray dot) during CPE at −2.20 V in 0.1 M ^{n}Bu$_4$NPF$_6$/DMF CO_2-saturated electrolyte.

chromatography (IC) were used to detect the products in the gas phase above the electrolysis cell and the electrolyte solution, respectively. The major products were identified as CO and CO_3^{2-} (Figures S32 and S33). The CO production was quantified at 250 μmol over 5 h by GC (Figure 3b), while the turnover number (TON) and the Faradaic Efficiency (FE) were calculated to be 50.2 and 91%, respectively (Table S5). Furthermore, the production of CO_3^{2-} was determined to be 267 μmol with a FE of 97% (Figure S33a). The measured quantity of CO_3^{2-} is marginally higher than that of CO, which can be attributed to the inherent deviation in the quantification of CO_3^{2-}.[6] Additionally, negligible amounts of H_2 and $HCOO^-$ were detected (Figures S32 and S34), which was presumed to be due to the trace amounts of H_2O in DMF. Gas chromatography−mass spectrometry (GC−MS) of CPE under a $^{13}CO_2$ atmosphere confirmed the formation of ^{13}CO (Figure S35). These results indicate that the reductive disproportionation of CO_2 occurs without the presence of a Brönsted acid. In contrast, CPE of 0.5 mM **Ni(hbpp)** under the same conditions resulted in an electrolysis current of only about 0.5 mA, and product analysis indicated the formation of merely 45 μmol CO and 49 μmol CO_3^{2-} (Figures 3b and S33b) over 5 h CPE with FEs of CO and CO_3^{2-} are 90% and 99%, respectively. These results illustrate that **Ni(hbpp)** is less active toward the electrocatalytic reduction of CO_2 compared to **NiNi(bphpp)**, suggesting that the secondary Ni site plays an important role in the catalytic process of CO_2 reduction disproportionation.

Confirmation of Homogeneous Catalysis

To confirm the homogeneous nature of the catalysis, stability tests of the catalysts were conducted to determine whether (a) the catalyst gradually decomposes throughout the CPE; and (b) the active heterogeneous materials form and attach to the electrode surface. Due to the large current when using the foamed graphite electrode, it is difficult to observe the difference before and after electrolysis. Consequently, a plate glassy carbon electrode was chosen as the working electrode. After 4 h CPE at −2.20 V, CV of 0.1 M ^{n}Bu$_4$NPF$_6$/DMF blank solution without either **NiNi(bphpp)** or **Ni(hbpp)** showed no obvious current change by using the plate glassy carbon electrode after rinse (Figure S36). Additionally, CVs of 0.5 mM **NiNi(bphpp)** or **Ni(hbpp)** solution after 4 h of CPE with the rinsed electrode displayed only minor differences compared to the CVs obtained before electrolysis with a fresh electrode (Figure S36). Further examination of the surface of the electrolyzed electrode through X-ray photoelectron spectroscopy (XPS) and scanning electron microscopy (SEM) revealed that the morphology and composition of rinsed plate glassy carbon electrode remained consistent with an unused electrode, with no visible heterogeneous materials detected (Figures S37 and S38). These findings strongly support the assertion that the catalysis processes involving **NiNi(bphpp)** and **Ni(hbpp)** are stable and homogeneous.

Kinetic Analysis

To intuitively assess the catalytic efficiency of **NiNi(bphpp)** and **Ni(hbpp)**, the foot of wave analysis (FOWA) method is applied to determine the turnover frequency (TOF).[124−126] Our results show that the calculated TOF of **NiNi(bphpp)**, derived from catalytic CV was 20.5 s^{-1}, while that of **Ni(hbpp)** was determined to be 4.4 s^{-1} (Table S6, Figures S39 and S40).[127] The improved TOF_{calc} obtained by the introduction of the secondary Ni site demonstrates the significant enhancement of catalytic activity through bimetallic cooperation.

Furthermore, the kinetics of electrocatalytic CO_2 reduction of **NiNi(bphpp)** and **Ni(hbpp)** were explored to understand the specific role of the secondary Ni site. The catalytic peak current (i_{cat}) of **NiNi(bphpp)** showed a linear relationship with its concentration (Figure S41), indicating the first-order kinetics of **NiNi(bphpp)**. Similarly, a linear relationship was observed between i_{cat} and the concentration of **Ni(hbpp)** (Figure S42). These findings suggest that both complexes facilitate CO_2 reduction as single molecules within the concentration range of 0−1.0 mM. However, the kinetic orders of CO_2 in the catalytic processes of the two catalysts differed markedly. Within the saturated range of CO_2 in DMF, the catalytic process of **NiNi(bphpp)** exhibited two distinct kinetic order regimes (Figures 4a and S43). At CO_2

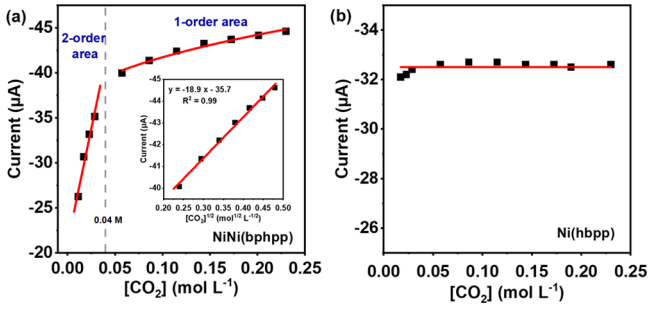

Figure 4. Relationship between i_{cat} and $[CO_2]$ of **NiNi(bphpp)** (a) and **Ni(hbpp)** (b) in the $[CO_2]$ range of 0−0.23 M. Inset: the relationship between i_{cat} and $[CO_2]^{1/2}$ of **NiNi(bphpp)** for the one-order area in (a).

concertation ($[CO_2]$) below 0.04 M, i_{cat} was directly proportional to the concentration of CO_2, indicating second-order kinetics. In contrast, i_{cat} correlated with the square root of CO_2 concentration ($[CO_2]^{1/2}$) between 0.04 and 0.23 M (Inset of Figure 4a), suggesting first-order kinetics. In comparison, in the saturated range of CO_2, the catalytic process of **Ni(hbpp)** followed zero-order kinetics (Figures 4b

https://doi.org/10.1021/jacsau.4c00047
JACS Au 2024, 4, 1207−1218

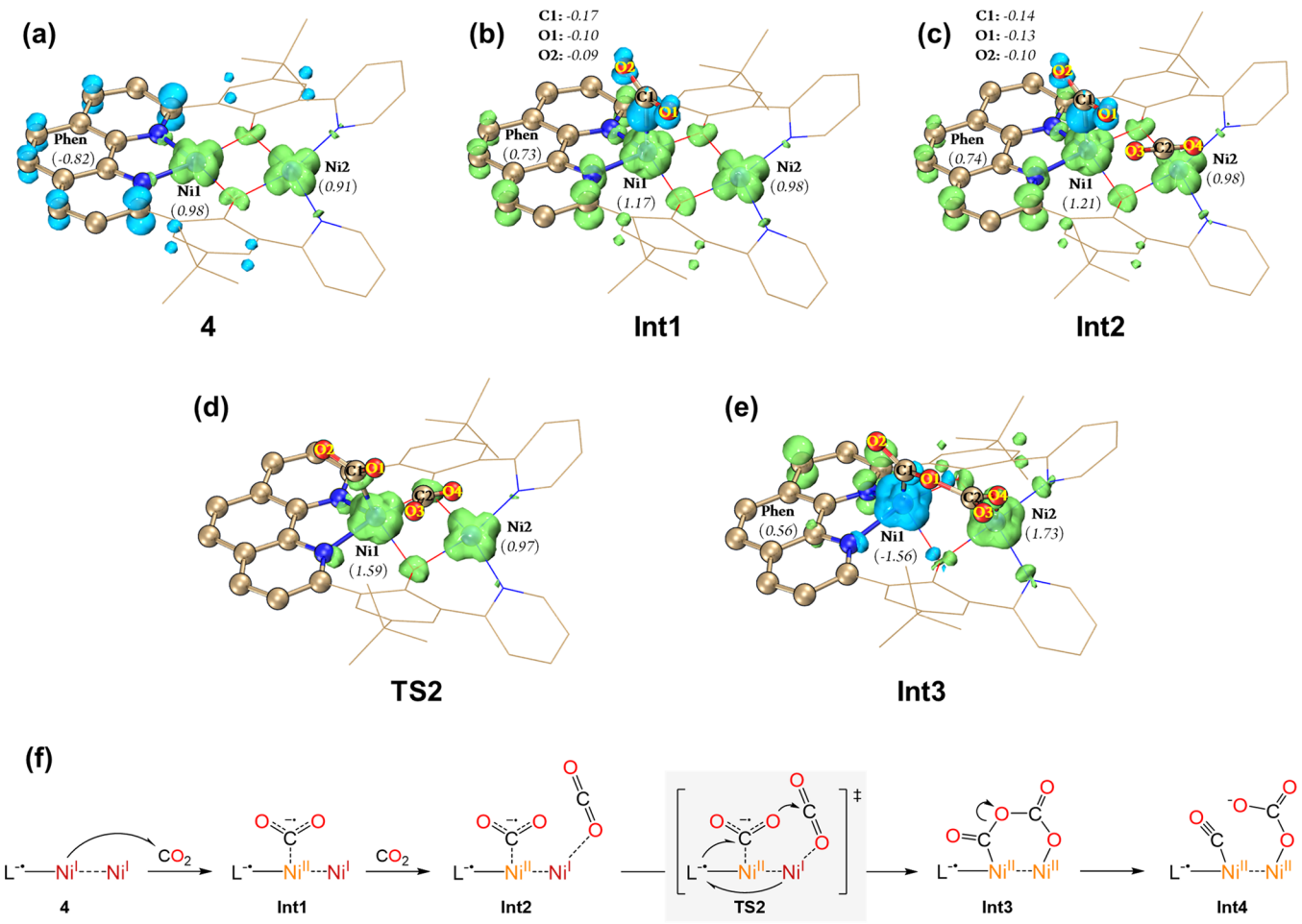

Figure 5. Spin population analysis (isovalue of 0.01) of **4** (a), **Int1** (b), **Int2** (c), **TS2** (d), and **Int3** (e) (**Phen** = phenanthroline) by Multiwfn[128] and VMD.[129] Green and blue isosurfaces represent α and β electrons, respectively. Spin population values are shown in italics. (f) The bimetallic cooperation mode of C−O bond activation and cleavage regulated by **NiNi(bphpp)**.

and S44). Considering the three key steps in the catalytic process of CO_2 reduction disproportionation (i.e., CO_2 binding, C−O bond activation, and C−O bond cleavage, eqs S5−S7),[8,111,123] it appears that **NiNi(bphpp)** presents a relatively low barrier of C−O bond cleavage; the CO_2 binding and C−O bond activation processes collectively dictate the catalytic rate at lower CO_2 concentration (eq S12), while C−O bond activation, which has a higher barrier, becomes more dominant as the concentration of CO_2 increases (eq S13). Conversely, the zero-order kinetics for **Ni(hbpp)** concerning $[CO_2]$ implies an extraordinarily high barrier of C−O bond cleavage, as CO_2 is not involved in this step (eq S14). Integrating with DFT study (discussed below and in Section 5 of the SI), the kinetic results strongly indicate that the secondary Ni site plays a private role in facilitating C−O bond activation and cleavage, thereby lowering the barriers in the catalytic cycle and potentially alerting the rate-determining step of the reaction. The augmented catalytic capability conferred by the well-integrated secondary Ni site was corroborated by the combined product analysis and the TOF and TON values. Additionally, a mixing experiment was conducted for further validation. Mixing **Ni(hbpp)** with an equivalent of $Ni(AcO)_2$ under identical electrochemical conditions does not result in any significant enhancement of the catalytic current (Figure S45).

Computational Studies

We further investigated the role of the secondary Ni site in enhancing the catalytic reduction of CO_2 using DFT calculations. The Gibbs free energy diagram (Figure S46) illustrates that CO_2 binding and subsequent chemical steps are facilitated following the formation of $Ni^INi^I(bphpp^{-\bullet})$ species **4** (Figure 5a). Under our inference, CO_2 binds readily to the Ni1 site, which is coordinated by reduced phenanthroline, thereby exhibiting increased nucleophilic character. This significant property is demonstrated by the low energy barrier associated with the reaction. Specifically, the Ni1−C1 bond forms via transition state **TS1**, with a remarkably low barrier of 3.8 kcal/mol, while the formation of the Ni2−C1 bond has a considerably higher barrier of 14.8 kcal/mol relative to species **4** (Figure S52), resulting in the generation of **Int1** (Figures 5b and S53). Interestingly, the Ni-CO_2 species within **Int1** presents a unique geometry, with a C1−O1 and C1−O2 distance of 1.21 Å, a Ni1−C1 distance of 2.094 Å, and an O1−C1−O2 angle of 146.9°. These parameters differ markedly from the previously reported structures of Ni^{II}-η^1-CO_2^{2-}-κC species which exhibit longer C−O distance (1.24−1.25 Å), shorter Ni−C distance (1.91−1.95 Å), and smaller angle of O−C−O (128−129°).[130,131] Hence, **Int1** represents a transitional configuration between Ni^{II}−CO_2 and Ni^{II}−CO_2^{2-}, presumably a Ni^{II}−$CO_2^{-\bullet}$ species. Moreover, during the formation of **Int1**, the spin population on Ni1 increases from

https://doi.org/10.1021/jacsau.4c00047
JACS Au 2024, 4, 1207−1218

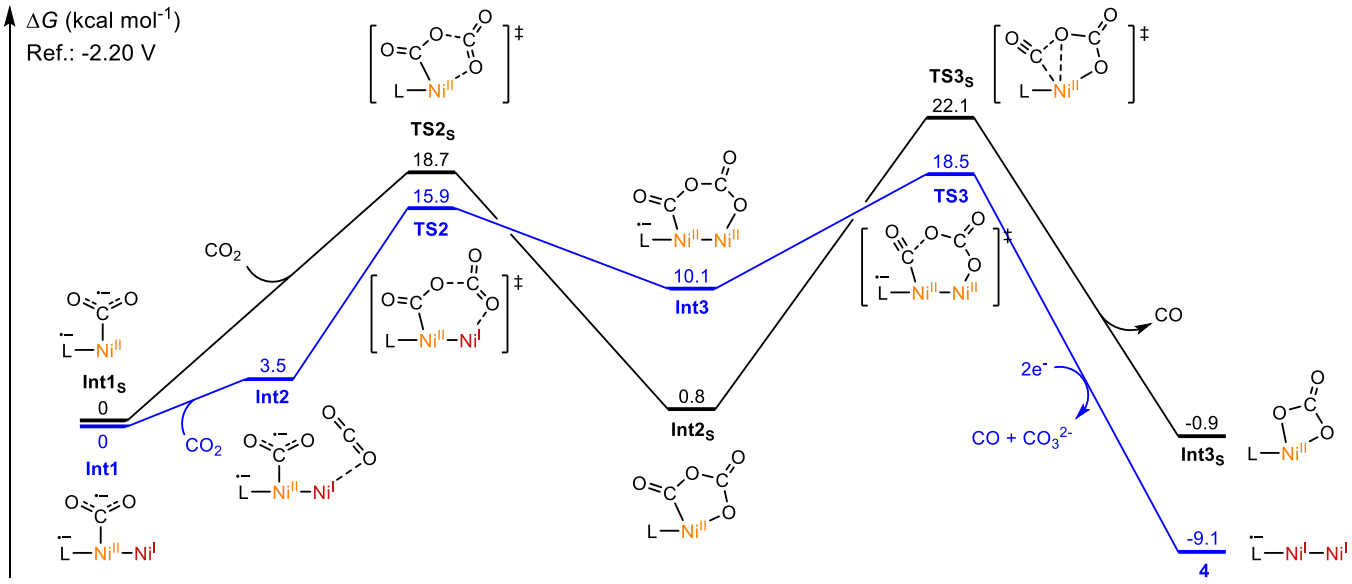

Figure 6. Calculated Gibbs free-energy diagrams of **NiNi(bphpp)** (blue line) and **Ni(hbpp)** (black line) starting at **Int1** and **Int1$_S$** at the B3LYP-D3/6-311+G(2df,2p)||B3LYP-D3/6-31G(d,p) level.

0.98 to 1.17, and the overall spin population on CO_2 increases to −0.363. This antiferromagnetic coupling with Ni1 gives rise to the distinct $Ni^{I}Ni^{II}(bphpp^{-\bullet})(CO_2^{-\bullet})$ species. Subsequently, **Int1** can attract another CO_2 molecule due to the impending nucleophilic attack of the O1 on C2, which carries an emerging negative charge, leading to the generation of intermediate **Int2** (Figures 5c and S53), where the O1−C2 distance is 2.79 Å.

Int2 subsequently initiates the critical C2−O1 bond formation between the $CO_2^{-\bullet}$ moiety and the second CO_2 with the notable assistance of Ni2. Within this cooperative context, the incoming CO_2 molecule can readily approach the reduced $CO_2^{-\bullet}$ and activate the C1−O1 bond through transition state **TS2** (Figures 5d and S54). The spin population of Ni1 increases from 1.21 to 1.59, while the spin population of phenanthroline decreases from 0.74 to 0.10, indicating an electron transfer from the phenanthroline ligand to the $CO_2^{-\bullet}$ moiety. Consequently, the resulting CO_2^{2-} unit can nucleophilically attack the adjacent CO_2 molecule with a relatively low barrier of 12.4 kcal/mol to **Int2** (Figure 6). Following this cooperative binding of activated CO_2 with additional CO_2, the $OCOCO_2^{2-}$ intermediate (**Int3**) is formed (Figures 5e and S55). Notably, the spin population of Ni2 increases from 0.97 in **TS2** to 1.73, whereas that of phenanthroline reverts to 0.56. This marked change in spin populations indicates an electron transfer from the Ni2(I) site to the phenanthroline, resulting in the formation of Ni2(II), which serves to stabilize the $OCOCO_2^{2-}$ anion with its Lewis acid character and culminates in the formation of the corresponding $Ni^{II}Ni^{II}(bphpp^{-\bullet})(OCOCO_2^{2-})$ species (**Int3**). In addition, the C1−O1 bond length gradually increases from 1.21 Å (**Int1**) to 1.22 Å (**Int2**), and finally to 1.44 Å (**Int3**), indicative of a typical C−O single bond. This bond activation process comprehensively corroborates the essential cooperative functions of the secondary Ni site (Figure 5f), which (a) acts as an electronic reservoir by storing the reduction equivalents, (b) facilitates the spatial approach of another CO_2 molecule as an electron mediator, thereby enabling electron transfers from reductive phenanthroline moiety to $CO_2^{-\bullet}$ moiety, and also from Ni2 to phenanthroline, and (c) stabilizes the $OCOCO_2^{2-}$ anion as a Lewis acid site.

Subsequently, the $OCOCO_2^{2-}$ unit within **Int3** can be converted into more thermodynamically stable species CO and CO_3^{2-} due to the cleavage of the C1−O1 bond. The CO−CO_3^{2-} cleavage occurs via a highly favorable transition state **TS3** (Figure S56), which is characterized by a comparatively lower barrier of 8.3 kcal/mol. This leads to the formation of a transient intermediate, termed **Int4** (Figure S57). The spin populations on Ni1, Ni2, and phenanthroline (1.26, 1.69, and 0.46, respectively) remain relatively unchanged from those of **Int3**, indicating a direct C−O cleavage process that results in the formation of the $Ni^{II}Ni^{II}(bphpp^{-\bullet})(CO)(CO_3^{2-})$ complex. This facile cleavage of the C−O bond is attributed to the Lewis acid character of Ni2, which also stabilizes the CO_3^{2-} unit (Figure 5f). Two pathways for the release of CO and CO_3^{2-} were considered, and both are considered plausible (Figure S46). Initially, the direct release pathway of either CO_3^{2-} or CO is endergonic by 17 or 0.6 kcal/mol, leading to the generation of **Int5** or **Int5′** (Figure S58), respectively. However, when coupled with a one-electron reduction, both processes become exergonic by −21.8 and −8 kcal/mol, resulting in the formation of **Int6** and **Int6′** (Figure S59), respectively. Although the prior release of CO_3^{2-} after a one-electron reduction is thermodynamically favorable, the subsequent reductive release of CO to complete the catalytic cycle is challenging due to the reduction potential of −2.12 V. In contrast, the reductive release of CO_3^{2-} from **Int6′** is facilitated by a lower potential of −1.52 V and returns to species **4**.

The importance of the secondary Ni site is further illustrated by the catalytic process of **Ni(hbpp)**, denoted as **1$_S$**. In contrast to **1**, the phenanthroline in **Ni(hbpp)** undergoes two consecutive one-electron reductions, resulting in the generations of **2$_S$** and **3$_S$**, respectively (Figure S60). The spin population of phenanthroline rises from 0 to 0.79 and then to 1.51, while that of Ni remains almost unchanged. The binding of CO_2 occurs via transition state **TS1$_S$** after the formation of **3$_S$** with a low barrier of 2.2 kcal/mol (Figures S47 and S61). Similar to **NiNi(bphpp)**, this process involves the one-electron

https://doi.org/10.1021/jacsau.4c00047
JACS Au 2024, 4, 1207−1218

activation of CO_2 with the generation of $Ni^{II}(hbpp^{-\bullet})(CO_2^{-\bullet})$, labeled as **Int1$_S$**, which has a relatively high reduction potential of −2.56 V (Figure S62). Thus, we inferred that **Int1$_S$** directly forms the C2−O1 bond with the second CO_2 molecule via transition state **TS2$_S$** (Figures 6 and S63), resulting in the generation of the five-membered ring intermediate, **Int2$_S$** (Figure S64). Without the cooperation of the secondary Ni site, the barrier of this bonding process is calculated to be 18.7 kcal/mol, which is 2.8 kcal/mol higher than that of **NiNi(bphpp)** (Figure 6). Subsequently, **Int2$_S$** undergoes C1−O1 cleavage via transition state **TS3$_S$** (Figure S65), followed by the departure of CO to generate $Ni^{II}(hbpp)(CO_3^{2-})$ intermediate **Int3$_S$** (Figure S66), which is exergonic by 23 kcal/mol (Figures 6 and S47). The barrier calculated for **TS3$_S$** is as high as 21.3 kcal/mol, which shows an obvious difference from the dinickel catalyst. For the transformation of **Int3** to **Int4** via **TS3**, Ni1(II) coordinated with reductive phenanthroline exhibits a certain nucleophilic character, which stabilizes the CO unit during C−O cleavage. In addition, Ni2(II) also stabilizes the CO_3^{2-} unit as a Lewis acid. This bimetallic cooperation results in a much lower barrier for the formation of **Int4**. However, compared with the only C−O bond cleavage in **TS3**, **TS3$_S$** involves both C−O bond cleavage and CO dissociation on a single Ni^{II} site, which is undoubtedly more kinetically unfavorable. The high C−O bond cleavage barrier for **TS3$_S$** also supports the zero-order kinetics of the catalytic process toward $[CO_2]$. Furthermore, the energetic span model (detailed in SI) is utilized to better describe the overall catalytic rate through the Gibbs free energy diagrams (Figures S46 and 47).[50,132,133] According to the model equation eq S15, the overall kinetic barrier (δE_{span}) for the **NiNi(bphpp)** catalytic cycle is calculated to be 19.3 kcal/mol, which is significantly lower than the δE_{span} value of 22.1 kcal/mol for the catalytic cycle of **Ni(hbpp)**. Using eq S16, the calculated TOF for **NiNi(bphpp)** catalysis is expected to be significantly higher than that of **Ni(hbpp)** catalysis. These theoretical results are completely consistent with the electrochemical properties, product characterizations, and catalytic kinetics of **NiNi(bphpp)** and **Ni(hbpp)**.

Both controlled experiments and DFT calculations have substantiated the pronounced enhancement of redox-active phenanthroline in facilitating CO_2 activation through coordinated Ni site, which avoids the generation of high-energy Ni^0 and contributes to the one-electron reduction of CO_2 to $CO_2^{-\bullet}$. Furthermore, the distinct roles of both Ni sites have been elucidated. Notably, the secondary Ni site actively aids in the activation of the C−O bond through "pre-coordination" with another CO_2 molecule as an important electron mediator. Additionally, the Lewis acid character of the secondary Ni site markedly facilitates the C−O bond cleavage, thereby promoting the entire catalytic process. This work emphasizes that bimetallic cooperation and redox-active ligand assistance are effective design strategies for the development of CO_2 reduction catalysts, even for the multielectron/proton redox catalysis of the other small molecules.[134−141]

CONCLUSIONS

Inspired by the catalytic mechanism of NiFe-CODH, this work explores the development of a binuclear Ni catalyst, **NiNi(bphpp)**, which enables bimetallic synergistic catalysis for CO_2 activation and catalytic conversion. By incorporating redox-active phenanthroline and a secondary Ni site, the bimetallic **NiNi(bphpp)** catalyst enables a three-electron reduction at a lower potential, leading to the generation of $Ni^{I}Ni^{I}(bphpp^{-\bullet})$ species. Subsequently, facile one-electron activation of CO_2 occurs, followed by activation and cleavage of the C−O bond through the coordination of a second CO_2 molecule. The involvement of the secondary Ni(I) site acts as an effective electron mediator, promoting electron transfer to the second CO_2 molecule and facilitating C−O bond activation. Furthermore, after formation of the $[OCOCO_2^{2-}]$ species, the secondary Ni(II) site exhibits Lewis acid characteristics, significantly aiding in C−O bond cleavage. These findings shed light on the distinct roles played by bimetallic sites in CO_2 reduction catalysis, providing insights into the nature of bimetallic cooperation. This work proposes new design strategies for catalysts in bimetallic synergistic multielectron catalytic processes. Based on this strategy, the development of the Ni−Fe heterobimetallic catalyst is in progress for efficient CO_2 reduction.

METHODS

All of the electrochemical experiments were conducted with a three-electrode system using a CHI-660E electrochemical workstation at room temperature. A glassy carbon electrode (GCE, 0.07 cm^2) was used as the working electrode, the counter electrode was a Pt wire, and $Ag/AgNO_3$ (0.1 M $AgNO_3$ in DMF) was used as the reference electrode and calibrated versus $Fc^{+/0}$. All of the reduction potentials were obtained from the DPVs of corresponding complexes. The gas above the electrolytic cell was drawn by a 1 mL Hamilton syringe and injected into the GC. CPE was conducted with 10 mL of 0.1 M $TBAPF_6$/DMF solution containing **NiNi(bphpp)** or **Ni(hbpp)** (0.5 mM) in a sealed standard three-electrode cell with stirring. A foamy carbon electrode (1.0 × 1.0 × 0.6 cm) was used as the working electrode. The Faraday efficiencies were calculated by the equation below:

$$FE = \frac{\text{moles of } CO_{exp}}{\text{moles of } CO_{CPE}}$$

$$CO_{CPE} = \frac{Q}{2F}$$

where CO_{exp} represents the CO content above the electrolytic cell which was determined by gas chromatography, and CO_{CPE} represents the CO content calculated from the total charge transfer (Q) during CPE (Figure S31).

ASSOCIATED CONTENT

Supporting Information

The Supporting Information is available free of charge at https://pubs.acs.org/doi/10.1021/jacsau.4c00047.

Additional experimental details, materials, methods, complex synthesis (^{1}H NMR and ESI-HRMS), magnetic property characterizations (Evans magnetic moment, EPR, and SQUID), X-ray crystallography, electrochemical studies, kinetic analysis, DFT calculations, and so on (PDF)

Accession Codes

CCDC 2257038, 2257041, 2257045, and 2257048 contain supplementary crystallographic data for this paper. These data can be obtained free of charge via www.ccdc.cam.ac.uk/data_request/cif, by emailing data_request@ccdc.cam.ac.uk, or by contacting The Cambridge Crystallographic Data Centre, 12 Union Road, Cambridge CB2 1EZ, UK; fax: +44 1223 336033.

https://doi.org/10.1021/jacsau.4c00047
JACS Au 2024, 4, 1207−1218

AUTHOR INFORMATION

Corresponding Author

Ming-Tian Zhang − *Center of Basic Molecular Science (CBMS), Department of Chemistry, Tsinghua University, Beijing 100084, China;* orcid.org/0000-0001-8808-9641; Email: mtzhang@mail.tsinghua.edu.cn

Authors

Yao Xiao − *Center of Basic Molecular Science (CBMS), Department of Chemistry, Tsinghua University, Beijing 100084, China*

Fei Xie − *Center of Basic Molecular Science (CBMS), Department of Chemistry, Tsinghua University, Beijing 100084, China*

Hong-Tao Zhang − *Center of Basic Molecular Science (CBMS), Department of Chemistry, Tsinghua University, Beijing 100084, China;* orcid.org/0000-0002-8237-9661

Complete contact information is available at: https://pubs.acs.org/10.1021/jacsau.4c00047

Notes

The authors declare no competing financial interest.

ACKNOWLEDGMENTS

We acknowledge the National Natural Science Foundation of China (NSFC 21933007 and 22193011) for funding support. We also appreciate Dr. Qiang Han for the support in ion chromatography analysis.

REFERENCES

(1) Lewis, N. S.; Nocera, D. G. Powering the planet: chemical challenges in solar energy utilization. *Proc. Natl. Acad. Sci. U. S. A.* **2006**, *103*, 15729−15735.

(2) Benson, E. E.; Kubiak, C. P.; Sathrum, A. J.; Smieja, J. M. Electrocatalytic and homogeneous approaches to conversion of CO_2 to liquid fuels. *Chem. Soc. Rev.* **2009**, *38*, 89−99.

(3) Appel, A. M.; Bercaw, J. E.; Bocarsly, A. B.; Dobbek, H.; DuBois, D. L.; Dupuis, M.; Ferry, J. G.; Fujita, E.; Hille, R.; Kenis, P. J. A.; Kerfeld, C. A.; Morris, R. H.; Peden, C. H.; Portis, A. R.; Ragsdale, S. W.; Rauchfuss, T. B.; Reek, J. N. H.; Seefeldt, L. C.; Thauer, R. K.; Waldrop, G. L. Frontiers, opportunities, and challenges in biochemical and chemical catalysis of CO_2 fixation. *Chem. Rev.* **2013**, *113*, 6621−6658.

(4) Francke, R.; Schille, B.; Roemelt, M. Homogeneously catalyzed electroreduction of carbon dioxide-methods, mechanisms, and catalysts. *Chem. Rev.* **2018**, *118*, 4631−4701.

(5) De Luna, P.; Hahn, C.; Higgins, D.; Jaffer, S. A.; Jaramillo, T. F.; Sargent, E. H. What would it take for renewably powered electrosynthesis to displace petrochemical processes? *Science* **2019**, *364*, No. eaav3506.

(6) Sullivan, B. P.; Bolinger, C. M.; Conrad, D.; Vining, W. J.; Meyer, T. J. One- and two-electron pathways in the electrocatalytic reduction of CO_2 by *fac*-Re(bpy)$(CO)_3$Cl (bpy = 2,2′-bipyridine). *J. Chem. Soc., Chem. Commun.* **1985**, 1414−1416.

(7) Keith, J. A.; Grice, K. A.; Kubiak, C. P.; Carter, E. A. Elucidation of the selectivity of proton-dependent electrocatalytic CO_2 reduction by *fac*-Re(bpy)$(CO)_3$Cl. *J. Am. Chem. Soc.* **2013**, *135*, 15823−15829.

(8) Machan, C. W.; Chabolla, S. A.; Yin, J.; Gilson, M. K.; Tezcan, F. A.; Kubiak, C. P. Supramolecular assembly promotes the electrocatalytic reduction of carbon dioxide by Re(I) bipyridine catalysts at a lower overpotential. *J. Am. Chem. Soc.* **2014**, *136*, 14598−14607.

(9) Sung, S.; Kumar, D.; Gil-Sepulcre, M.; Nippe, M. Electrocatalytic CO_2 reduction by imidazolium-functionalized molecular catalysts. *J. Am. Chem. Soc.* **2017**, *139*, 13993−13996.

(10) Haviv, E.; Azaiza-Dabbah, D.; Carmieli, R.; Avram, L.; Martin, J. M. L.; Neumann, R. A thiourea tether in the second coordination sphere as a binding site for CO_2 and a proton donor promotes the electrochemical reduction of CO_2 to CO catalyzed by a rhenium bipyridine-type complex. *J. Am. Chem. Soc.* **2018**, *140*, 12451−12456.

(11) Slater, S.; Wagenknecht, J. H. Electrochemical reduction of carbon dioxide catalyzed by Rh$(diphos)_2$Cl. *J. Am. Chem. Soc.* **1984**, *106*, 5367−5368.

(12) Bolinger, C. M.; Story, N.; Sullivan, B. P.; Meyer, T. J. Electrocatalytic reduction of carbon dioxide by 2,2′-bipyridine complexes of rhodium and iridium. *Inorg. Chem.* **1988**, *27*, 4582−4587.

(13) Todorova, T. K.; Huan, T. N.; Wang, X.; Agarwala, H.; Fontecave, M. Controlling hydrogen evolution during photoreduction of CO_2 to formic acid using $[Rh(R\text{-}bpy)(Cp^*)Cl]^+$ catalysts: a structure-activity study. *Inorg. Chem.* **2019**, *58*, 6893−6903.

(14) Ishida, H.; Tanaka, H.; Tanaka, K.; Tanaka, T. Selective formation of $HCOO^-$ in the electrochemical CO_2 reduction catalysed by $[Ru(bpy)_2(CO)_2]^{2+}$ (bpy = 2,2′-bipyridine). *J. Chem. Soc., Chem. Commun.* **1987**, 131−132.

(15) Mizukawa, T.; Tsuge, K.; Nakajima, H.; Tanaka, K. Selective production of acetone in the electrochemical reduction of CO_2 catalyzed by a Ru-naphthyridine complex. *Angew. Chem., Int. Ed.* **1999**, *38*, 362−363.

(16) Boston, D. J.; Pachón, Y. M.; Lezna, R. O.; de Tacconi, N. R.; MacDonnell, F. M. Electrocatalytic and photocatalytic conversion of CO_2 to methanol using ruthenium complexes with internal pyridyl cocatalysts. *Inorg. Chem.* **2014**, *53*, 6544−6553.

(17) Machan, C. W.; Sampson, M. D.; Kubiak, C. P. A molecular ruthenium electrocatalyst for the reduction of carbon dioxide to CO and formate. *J. Am. Chem. Soc.* **2015**, *137*, 8564−8571.

(18) Johnson, B. A.; Maji, S.; Agarwala, H.; White, T. A.; Mijangos, E.; Ott, S. Activating a low overpotential CO_2 reduction mechanism by a strategic ligand modification on a ruthenium polypyridyl catalyst. *Angew. Chem., Int. Ed.* **2016**, *55*, 1825−1829.

(19) Ono, T.; Qu, S.; Gimbert-Suriñach, C.; Johnson, M. A.; Marell, D. J.; Benet-Buchholz, J.; Cramer, C. J.; Llobet, A. Hydrogenative carbon dioxide reduction catalyzed by mononuclear ruthenium polypyridyl complexes: discerning between electronic and steric effects. *ACS Catal.* **2017**, *7*, 5932−5940.

(20) Gonell, S.; Massey, M. D.; Moseley, I. P.; Schauer, C. K.; Muckerman, J. T.; Miller, A. J. M. The *trans* effect in electrocatalytic CO_2 reduction: mechanistic studies of asymmetric ruthenium pyridyl-carbene catalysts. *J. Am. Chem. Soc.* **2019**, *141*, 6658−6671.

(21) Sampaio, R. N.; Grills, D. C.; Polyansky, D. E.; Szalda, D. J.; Fujita, E. Unexpected roles of triethanolamine in the photochemical reduction of CO_2 to formate by ruthenium complexes. *J. Am. Chem. Soc.* **2020**, *142*, 2413−2428.

(22) Agarwala, H.; Chen, X.; Lyonnet, J. R.; Johnson, B. A.; Ahlquist, M.; Ott, S. Alternating metal-ligand coordination improves electrocatalytic CO_2 reduction by a mononuclear Ru catalyst. *Angew. Chem., Int. Ed.* **2023**, *62*, No. e202218728.

(23) Hunt, L. A.; Das, S.; Lamb, R. W.; Nugegoda, D.; Curiac, C.; Figgins, M. T.; Lambert, E. C.; Qu, F.; Hammer, N. I.; Delcamp, J. H.; Webster, C. E.; Papish, E. T. Ruthenium (II) complexes of CNC pincers and bipyridine in the photocatalytic CO_2 reduction reaction to CO using visible light: catalysis, kinetics, and computational insights. *ACS Catal.* **2023**, *13*, 5986−5999.

(24) Hammouche, M.; Lexa, D.; Savéant, J. M.; Momenteau, M. Catalysis of the electrochemical reduction of carbon dioxide by iron("0") porphyrins. *J. Electroanal. Chem.* **1988**, *249*, 347−351.

(25) Costentin, C.; Drouet, S.; Robert, M.; Savéant, J.-M. A local proton source enhances CO_2 electroreduction to CO by a molecular Fe catalyst. *Science* **2012**, *338*, 90−94.

(26) Chen, L.; Guo, Z.; Wei, X. G.; Gallenkamp, C.; Bonin, J.; Anxolabéhère-Mallart, E.; Lau, K.-C.; Lau, T.-C.; Robert, M. Molecular catalysis of the electrochemical and photochemical reduction of CO_2 with earth-abundant metal complexes. selective

production of CO vs HCOOH by switching of the metal center. *J. Am. Chem. Soc.* **2015**, *137*, 10918−10921.
(27) Azcarate, I.; Costentin, C.; Robert, M.; Savéant, J. M. Through-space charge interaction substituent effects in molecular catalysis leading to the design of the most efficient catalyst of CO_2-to-CO electrochemical conversion. *J. Am. Chem. Soc.* **2016**, *138*, 16639−16644.
(28) Rao, H.; Schmidt, L. C.; Bonin, J.; Robert, M. Visible-light-driven methane formation from CO_2 with a molecular iron catalyst. *Nature* **2017**, *548*, 74−77.
(29) Margarit, C. G.; Schnedermann, C.; Asimow, N. G.; Nocera, D. G. Carbon dioxide reduction by iron hangman porphyrins. *Organometallics* **2019**, *38*, 1219−1223.
(30) Derrick, J. S.; Loipersberger, M.; Chatterjee, R.; Iovan, D. A.; Smith, P. T.; Chakarawet, K.; Yano, J.; Long, J. R.; Head-Gordon, M.; Chang, C. J. Metal−ligand cooperativity via exchange coupling promotes iron-catalyzed electrochemical CO_2 reduction at low overpotentials. *J. Am. Chem. Soc.* **2020**, *142*, 20489−20501.
(31) Martin, D. J.; Mayer, J. M. Oriented electrostatic effects on O_2 and CO_2 reduction by a polycationic iron porphyrin. *J. Am. Chem. Soc.* **2021**, *143*, 11423−11434.
(32) Wang, X.-Z.; Meng, S.-L.; Chen, J.-Y.; Wang, H.-X.; Wang, Y.; Zhou, S.; Li, X.-B.; Liao, R.-Z.; Tung, C.-H.; Wu, L.-Z. Mechanistic insights into iron(II) bis(pyridyl)amine-bipyridine skeleton for selective CO_2 photoreduction. *Angew. Chem., Int. Ed.* **2021**, *60*, 26072−26079.
(33) Amanullah, S.; Saha, P.; Dey, A. Activating the Fe(I) state of iron porphyrinoid with second-sphere proton transfer residues for selective reduction of CO_2 to HCOOH via Fe(III/II)-COOH intermediate(s). *J. Am. Chem. Soc.* **2021**, *143*, 13579−13592.
(34) Massie, A. A.; Schremmer, C.; Rüter, I.; Dechert, S.; Siewert, I.; Meyer, F. Selective electrocatalytic CO_2 reduction to CO by an NHC-based organometallic heme analogue. *ACS Catal.* **2021**, *11*, 3257−3267.
(35) Guo, K.; Li, X.; Lei, H.; Guo, H.; Jin, X.; Zhang, X.-P.; Zhang, W.; Apfel, U.-P.; Cao, R. Role-specialized division of labor in CO_2 reduction with doubly-functionalized iron porphyrin atropisomers. *Angew. Chem., Int. Ed.* **2022**, *61*, No. e202209602.
(36) Derrick, J. S.; Loipersberger, M.; Nistanaki, S. K.; Rothweiler, A. V.; Head-Gordon, M.; Nichols, E. M.; Chang, C. J. Templating bicarbonate in the second coordination sphere enhances electrochemical CO_2 reduction catalyzed by iron porphyrins. *J. Am. Chem. Soc.* **2022**, *144*, 11656−11663.
(37) Pugliese, E.; Gotico, P.; Wehrung, I.; Boitrel, B.; Quaranta, A.; Ha-Thi, M. H.; Pino, T.; Sircoglou, M.; Leibl, W.; Halime, Z.; Aukauloo, A. Dissection of light-induced charge accumulation at a highly active iron porphyrin: insights in the photocatalytic CO_2 reduction. *Angew. Chem., Int. Ed.* **2022**, *61*, No. e202117530.
(38) Fisher, B.; Eisenberg, R. Electrocatalytic reduction of carbon dioxide by using macrocycles of nickel and cobalt. *J. Am. Chem. Soc.* **1980**, *102*, 7361−7363.
(39) Beley, M.; Collin, J. P.; Ruppert, R.; Sauvage, J. P. Electrocatalytic reduction of CO_2 by Ni cyclam^{2+} in water: study of the factors affecting the efficiency and the selectivity of the process. *J. Am. Chem. Soc.* **1986**, *108*, 7461−7467.
(40) Rudolph, M.; Dautz, S.; Jäger, E.-G. Macrocyclic [N_4^{2-}] coordinated nickel complexes as catalysts for the formation of oxalate by electrochemical reduction of carbon dioxide. *J. Am. Chem. Soc.* **2000**, *122*, 10821−10830.
(41) Thoi, V. S.; Kornienko, N.; Margarit, C. G.; Yang, P.; Chang, C. J. Visible-light photoredox catalysis: selective reduction of carbon dioxide to carbon monoxide by a nickel *N*-heterocyclic carbene-isoquinoline complex. *J. Am. Chem. Soc.* **2013**, *135*, 14413−14424.
(42) Froehlich, J. D.; Kubiak, C. P. The homogeneous reduction of CO_2 by [Ni(cyclam)]$^+$: increased catalytic rates with the addition of a CO scavenger. *J. Am. Chem. Soc.* **2015**, *137*, 3565−3573.
(43) Hong, D.; Tsukakoshi, Y.; Kotani, H.; Ishizuka, T.; Kojima, T. Visible-light-driven photocatalytic CO_2 reduction by a Ni(II) complex bearing a bioinspired tetradentate ligand for selective CO production. *J. Am. Chem. Soc.* **2017**, *139*, 6538−6541.
(44) Shirley, H.; Su, X.; Sanjanwala, H.; Talukdar, K.; Jurss, J. W.; Delcamp, J. H. Durable solar-powered systems with Ni-catalysts for conversion of CO_2 or CO to CH_4. *J. Am. Chem. Soc.* **2019**, *141*, 6617−6622.
(45) Lacy, D. C.; McCrory, C. C.; Peters, J. C. Studies of cobalt-mediated electrocatalytic CO_2 reduction using a redox-active ligand. *Inorg. Chem.* **2014**, *53*, 4980−4988.
(46) Shaffer, D. W.; Johnson, S. I.; Rheingold, A. L.; Ziller, J. W.; Goddard, W. A., III; Nielsen, R. J.; Yang, J. Y. Reactivity of a series of isostructural cobalt pincer complexes with CO_2, CO, and H^+. *Inorg. Chem.* **2014**, *53*, 13031−13041.
(47) Chapovetsky, A.; Do, T. H.; Haiges, R.; Takase, M. K.; Marinescu, S. C. Proton-assisted reduction of CO_2 by cobalt aminopyridine macrocycles. *J. Am. Chem. Soc.* **2016**, *138*, 5765−5768.
(48) Guo, Z.; Cheng, S.; Cometto, C.; Anxolabéhère-Mallart, E.; Ng, S.-M.; Ko, C.-C.; Liu, G.; Chen, L.; Robert, M.; Lau, T.-C. Highly efficient and selective photocatalytic CO_2 Reduction by iron and cobalt quaterpyridine complexes. *J. Am. Chem. Soc.* **2016**, *138*, 9413−9416.
(49) Roy, S.; Sharma, B.; Pecaut, J.; Simon, P.; Fontecave, M.; Tran, P. D.; Derat, E.; Artero, V. Molecular cobalt complexes with pendant amines for selective electrocatalytic reduction of carbon dioxide to formic acid. *J. Am. Chem. Soc.* **2017**, *139*, 3685−3696.
(50) Fernández, S.; Franco, F.; Casadevall, C.; Martin-Diaconescu, V.; Luis, J. M.; Lloret-Fillol, J. A unified electro- and photocatalytic CO_2 to CO reduction mechanism with aminopyridine cobalt complexes. *J. Am. Chem. Soc.* **2020**, *142*, 120−133.
(51) Dey, S.; Todorova, T. K.; Fontecave, M.; Mougel, V. Electroreduction of CO_2 to formate with low overpotential using cobalt pyridine thiolate complexes. *Angew. Chem., Int. Ed.* **2020**, *59*, 15726−15733.
(52) Queyriaux, N.; Abel, K.; Fize, J.; Pécaut, J.; Orio, M.; Hammarström, L. From non-innocent to guilty: on the role of redox-active ligands in the electro-assisted reduction of CO_2 mediated by a cobalt(II)-polypyridyl complex. *Sustainable Energy Fuels* **2020**, *4*, 3668−3676.
(53) Zhang, X.; Yamauchi, K.; Sakai, K. Earth-abundant photocatalytic CO_2 reduction by multielectron chargeable cobalt porphyrin catalysts: high CO/H_2 selectivity in water based on phase mismatch in frontier MO association. *ACS Catal.* **2021**, *11*, 10436−10449.
(54) Loipersberger, M.; Cabral, D. G. A.; Chu, D. B. K.; Head-Gordon, M. Mechanistic insights into Co and Fe quaterpyridine-based CO_2 reduction catalysts: metal-ligand orbital interaction as the key driving force for distinct pathways. *J. Am. Chem. Soc.* **2021**, *143*, 744−763.
(55) Wang, X. S.; Yang, J. Y. Translating aqueous CO_2 hydrogenation activity to electrocatalytic reduction with a homogeneous cobalt catalyst. *Chem. Commun.* **2023**, *59*, 338−341.
(56) Bourrez, M.; Molton, F.; Chardon-Noblat, S.; Deronzier, A. [Mn(bipyridyl)$(CO)_3$Br]: an abundant metal carbonyl complex as efficient electrocatalyst for CO_2 reduction. *Angew. Chem., Int. Ed.* **2011**, *50*, 9903−9906.
(57) Sampson, M. D.; Nguyen, A. D.; Grice, K. A.; Moore, C. E.; Rheingold, A. L.; Kubiak, C. P. Manganese catalysts with bulky bipyridine ligands for the electrocatalytic reduction of carbon dioxide: eliminating dimerization and altering catalysis. *J. Am. Chem. Soc.* **2014**, *136*, 5460−5471.
(58) Agarwal, J.; Shaw, T. W.; Stanton, C. J., III; Majetich, G. F.; Bocarsly, A. B.; Schaefer, H. F., III NHC-containing manganese(I) electrocatalysts for the two-electron reduction of CO_2. *Angew. Chem., Int. Ed.* **2014**, *53*, 5152−5155.
(59) Ngo, K. T.; McKinnon, M.; Mahanti, B.; Narayanan, R.; Grills, D. C.; Ertem, M. Z.; Rochford, J. Turning on the protonation-first pathway for electrocatalytic CO_2 reduction by manganese bipyridyl tricarbonyl complexes. *J. Am. Chem. Soc.* **2017**, *139*, 2604−2618.
(60) Franco, F.; Pinto, M. F.; Royo, B.; Lloret-Fillol, J. A highly active N-heterocyclic carbene manganese(I) complex for selective

https://doi.org/10.1021/jacsau.4c00047
JACS Au 2024, 4, 1207−1218

electrocatalytic CO_2 reduction to CO. *Angew. Chem., Int. Ed.* **2018**, *57*, 4603−4606.
(61) Sung, S.; Li, X.; Wolf, L. M.; Meeder, J. R.; Bhuvanesh, N. S.; Grice, K. A.; Panetier, J. A.; Nippe, M. Synergistic effects of imidazolium-functionalization on *fac*-$Mn(CO)_3$ bipyridine catalyst platforms for electrocatalytic carbon dioxide reduction. *J. Am. Chem. Soc.* **2019**, *141*, 6569−6582.
(62) Rønne, M. H.; Cho, D.; Madsen, M. R.; Jakobsen, J. B.; Eom, S.; Escoudé, É.; Hammershøj, H. C. D.; Nielsen, D. U.; Pedersen, S. U.; Baik, M.-H.; Skrydstrup, T.; Daasbjerg, K. Ligand-controlled product selectivity in electrochemical carbon dioxide reduction using manganese bipyridine catalysts. *J. Am. Chem. Soc.* **2020**, *142*, 4265−4275.
(63) Yang, Y.; Ertem, M. Z.; Duan, L. An amide-based second coordination sphere promotes the dimer pathway of Mn-catalyzed CO_2-to-CO reduction at low overpotential. *Chem. Sci.* **2021**, *12*, 4779−4788.
(64) Tory, J.; Setterfield-Price, B.; Dryfe, R. A. W.; Hartl, F. $[M(CO)_4$ (2,2'-bipyridine)] (M = Cr, Mo, W) complexes as efficient catalysts for electrochemical reduction of CO_2 at a gold electrode. *ChemElectroChem.* **2015**, *2*, 213−217.
(65) Hooe, S. L.; Moreno, J. J.; Reid, A. G.; Cook, E. N.; Machan, C. W. Mediated inner-sphere electron transfer induces homogeneous reduction of CO_2 via through-space electronic conjugation. *Angew. Chem., Int. Ed.* **2022**, *61*, No. e202109645.
(66) DuBois, D. L.; Miedaner, A.; Haltiwanger, R. C. Electrochemical reduction of carbon dioxide catalyzed by [Pd(triphosphine)(solvent)]$(BF_4)_2$ complexes: synthetic and mechanistic studies. *J. Am. Chem. Soc.* **1991**, *113*, 8753−8764.
(67) Therrien, J. A.; Wolf, M. O.; Patrick, B. O. Electrocatalytic reduction of CO_2 with palladium bis-N-heterocyclic carbene pincer complexes. *Inorg. Chem.* **2014**, *53*, 12962−12972.
(68) Buss, J. A.; VanderVelde, D. G.; Agapie, T. Lewis acid enhancement of proton induced CO_2 cleavage: Bond weakening and ligand residence time effects. *J. Am. Chem. Soc.* **2018**, *140*, 10121−10125.
(69) Cunningham, D. W.; Barlow, J. M.; Velazquez, R. S.; Yang, J. Y. Reversible and selective CO_2 to HCO_2^- electrocatalysis near the thermodynamic potential. *Angew. Chem., Int. Ed.* **2020**, *59*, 4443−4447.
(70) Ceballos, B. M.; Yang, J. Y. Highly selective electrocatalytic CO_2 reduction by $[Pt(dmpe)_2]^{2+}$ through kinetic and thermodynamic control. *Organometallics* **2020**, *39*, 1491−1496.
(71) Costentin, C.; Robert, M.; Savéant, J. M. Current issues in molecular catalysis illustrated by iron porphyrins as catalysts of the CO_2-to-CO electrochemical conversion. *Acc. Chem. Res.* **2015**, *48*, 2996−3006.
(72) Amanullah, S.; Saha, P.; Nayek, A.; Ahmed, M. E.; Dey, A. Biochemical and artificial pathways for the reduction of carbon dioxide, nitrite and the competing proton reduction: effect of 2nd sphere interactions in catalysis. *Chem. Soc. Rev.* **2021**, *50*, 3755−3823.
(73) Fujita, E.; Grills, D. C.; Manbeck, G. F.; Polyansky, D. E. Understanding the role of inter- and intramolecular promoters in electro- and photochemical CO_2 reduction using Mn, Re, and Ru catalysts. *Acc. Chem. Res.* **2022**, *55*, 616−628.
(74) Saha, P.; Amanullah, S.; Dey, A. Selectivity in electrochemical CO_2 reduction. *Acc. Chem. Res.* **2022**, *55*, 134−144.
(75) Shin, W.; Lindahl, P. A. Function and CO binding properties of the NiFe complex in carbon monoxide dehydrogenase from *Clostridium thermoaceticum*. *Biochemistry* **1992**, *31*, 12870−12875.
(76) Ragsdale, S. W.; Kumar, M. Nickel-containing carbon monoxide dehydrogenase/acetyl-CoA synthase. *Chem. Rev.* **1996**, *96*, 2515−2539.
(77) Gong, W.; Hao, B.; Wei, Z.; Ferguson, D. J., Jr.; Tallant, T.; Krzycki, J. A.; Chan, M. K. Structure of the $\alpha 2\varepsilon 2$ Ni-dependent CO dehydrogenase component of the *Methanosarcina barkeri* acetyl-CoA decarbonylase/synthase complex. *Proc. Natl. Acad. Sci. U. S. A.* **2008**, *105*, 9558−9563.
(78) Can, M.; Armstrong, F. A.; Ragsdale, S. W. Structure, function, and mechanism of the nickel metalloenzymes, CO dehydrogenase, and acetyl-CoA synthase. *Chem. Rev.* **2014**, *114*, 4149−4174.
(79) Stripp, S. T.; Duffus, B. R.; Fourmond, V.; Léger, C.; Leimkühler, S.; Hirota, S.; Hu, Y.; Jasniewski, A.; Ogata, H.; Ribbe, M. W. Second and outer coordination sphere effects in nitrogenase, hydrogenase, formate dehydrogenase, and CO dehydrogenase. *Chem. Rev.* **2022**, *122*, 11900−11973.
(80) Basak, Y.; Jeoung, J. H.; Domnik, L.; Dobbek, H. Stepwise O_2-induced rearrangement and disassembly of the $[NiFe_4(OH)(\mu_3\text{-}S)_4]$ active site cluster of CO dehydrogenase. *Angew. Chem., Int. Ed.* **2023**, *62*, No. e202305341.
(81) Dobbek, H.; Svetlitchnyi, V.; Gremer, L.; Huber, R.; Meyer, O. Crystal structure of a carbon monoxide dehydrogenase reveals a [Ni-4Fe-5S] cluster. *Science* **2001**, *293*, 1281−1285.
(82) Dobbek, H.; Svetlitchnyi, V.; Liss, J.; Meyer, O. Carbon monoxide induced decomposition of the active site [Ni-4Fe-5S] cluster of CO dehydrogenase. *J. Am. Chem. Soc.* **2004**, *126*, 5382−5387.
(83) Jeoung, J. H.; Dobbek, H. Carbon dioxide activation at the Ni,Fe-cluster of anaerobic carbon monoxide dehydrogenase. *Science* **2007**, *318*, 1461−1464.
(84) Haines, R. J.; Wittrig, R. E.; Kubiak, C. P. Electrocatalytic reduction of carbon dioxide by the binuclear copper complex $[Cu_2(6\text{-}(diphenylphosphino)\text{-}2,2'\text{-}bipyridyl)_2(MeCN)_2][PF_6]_2$. *Inorg. Chem.* **1994**, *33*, 4723−4728.
(85) Steffey, B. D.; Curtis, C. J.; Dubois, D. L. Electrochemical reduction of CO_2 catalyzed by a dinuclear palladium complex containing a bridging hexaphosphine ligand: evidence for cooperativity. *Organometallics* **1995**, *14*, 4937−4943.
(86) Ali, M. M.; Sato, H.; Mizukawa, T.; Tsuge, K.; Haga, M.; Tanaka, K. Selective formation of HCO_2^- and $C_2O_4^{2-}$ in electrochemical reduction of CO_2 catalyzed by mono- and di-nuclear ruthenium complexes. *Chem. Commun.* **1998**, 249−250.
(87) Raebiger, J. W.; Turner, J. W.; Noll, B. C.; Curtis, C. J.; Miedaner, A.; Cox, B.; DuBois, D. L. Electrochemical reduction of CO_2 to CO catalyzed by a bimetallic palladium complex. *Organometallics* **2006**, *25*, 3345−3351.
(88) Angamuthu, R.; Byers, P.; Lutz, M.; Spek, A. L.; Bouwman, E. Electrocatalytic CO_2 conversion to oxalate by a copper complex. *Science* **2010**, *327*, 313−315.
(89) Mohamed, E. A.; Zahran, Z. N.; Naruta, Y. Efficient electrocatalytic CO_2 reduction with a molecular cofacial iron porphyrin dimer. *Chem. Commun.* **2015**, *51*, 16900−16903.
(90) Witt, S. E.; White, T. A.; Li, Z.; Dunbar, K. R.; Turro, C. Cationic dirhodium(II,II) complexes for the electrocatalytic reduction of CO_2 to HCOOH. *Chem. Commun.* **2016**, *52*, 12175−12178.
(91) Ouyang, T.; Huang, H. H.; Wang, J. W.; Zhong, D. C.; Lu, T. B. A dinuclear cobalt cryptate as a homogeneous photocatalyst for highly selective and efficient visible-light driven CO_2 reduction to CO in CH_3CN/H_2O solution. *Angew. Chem., Int. Ed.* **2017**, *56*, 738−743.
(92) Cao, L.-M.; Huang, H.-H.; Wang, J.-W.; Zhong, D.-C.; Lu, T.-B. The synergistic catalysis effect within a dinuclear nickel complex for efficient and selective electrocatalytic reduction of CO_2 to CO. *Green Chem.* **2018**, *20*, 798−803.
(93) Cheng, M.; Yu, Y.; Zhou, X.; Luo, Y.; Wang, M. Chemical versatility of [FeFe]-hydrogenase models: distinctive activity of $[\mu\text{-}C_6H_4\text{-}1,2\text{-}(\kappa^2\text{-}S)_2][Fe_2(CO)_6]$ for electrocatalytic CO_2 reduction. *ACS Catal.* **2019**, *9*, 768−774.
(94) Ouyang, T.; Wang, H.-J.; Huang, H.-H.; Wang, J.-W.; Guo, S.; Liu, W.-J.; Zhong, D.-C.; Lu, T.-B. Dinuclear metal synergistic catalysis boosts photochemical CO_2-to-CO conversion. *Angew. Chem., Int. Ed.* **2018**, *57*, 16480−16485.
(95) Yang, W.; Sinha Roy, S.; Pitts, W. C.; Nelson, R. L.; Fronczek, F. R.; Jurss, J. W. Electrocatalytic CO_2 reduction with *cis* and *trans* conformers of a rigid dinuclear rhenium complex: Comparing the monometallic and cooperative bimetallic pathways. *Inorg. Chem.* **2018**, *57*, 9564−9575.

https://doi.org/10.1021/jacsau.4c00047
JACS Au 2024, 4, 1207−1218

(96) Guo, Z.; Chen, G.; Cometto, C.; Ma, B.; Zhao, H.; Groizard, T.; Chen, L.; Fan, H.; Man, W.-L.; Yiu, S.-M.; Lau, K.-C.; Lau, T.-C.; Robert, M. Selectivity control of CO versus $HCOO^-$ production in the visible-light-driven catalytic reduction of CO_2 with two cooperative metal sites. *Nat. Catal.* **2019**, *2*, 801−808.
(97) Ahmed, M. E.; Adam, S.; Saha, D.; Fize, J.; Artero, V.; Dey, A.; Duboc, C. Repurposing a bio-inspired NiFe hydrogenase model for CO_2 reduction with selective production of methane as the unique C-based product. *ACSEnergy Lett.* **2020**, *5*, 3837−3842.
(98) Polyansky, D. E.; Grills, D. C.; Ertem, M. Z.; Ngo, K. T.; Fujita, E. Role of bimetallic interactions in the enhancement of catalytic CO_2 reduction by a macrocyclic cobalt catalyst. *ACS Catal.* **2022**, *12*, 1706−1717.
(99) Zhang, C.; Gotico, P.; Guillot, R.; Dragoe, D.; Leibl, W.; Halime, Z.; Aukauloo, A. Bio-inspired bimetallic cooperativity through a hydrogen bonding spacer in CO_2 reduction. *Angew. Chem., Int. Ed.* **2023**, *62*, No. e202214665.
(100) Ciurli, S.; Ross, P. K.; Scott, M. J.; Yu, S.-B.; Holm, R. H. Synthetic nickel-containing heterometal cubane-type clusters with $NiFe_3Q_4$ cores (Q = S, Se). *J. Am. Chem. Soc.* **1992**, *114*, 5415−5423.
(101) Tan, G. O.; Ensign, S. A.; Ciurli, S.; Scott, M. J.; Hedman, B.; Holm, R. H.; Ludden, P. W.; Korszun, Z. R.; Stephens, P. J.; Hodgson, K. O. On the structure of the nickel/iron/sulfur center of the carbon monoxide dehydrogenase from *Rhodospirillum rubrum*: an X-ray absorption spectroscopy study. *Proc. Natl. Acad. Sci. U. S. A.* **1992**, *89*, 4427−4431.
(102) Zhou, J.; Scott, M. J.; Hu, Z.; Peng, G.; Munck, E.; Holm, R. H. Synthesis and comparative reactivity and electronic structural features of $[MFe_3S_4]^{z+}$ cubane-type clusters (M = Fe, Co, Ni). *J. Am. Chem. Soc.* **1992**, *114*, 10843−10854.
(103) Osterloh, F.; Saak, W.; Pohl, S. Unidentate and bidentate binding of nickel(II) complexes to an Fe_4S_4 cluster *via* bridging thiolates: Synthesis, crystal structures, and electrochemical properties of model compounds for the active sites of nickel containing CO dehydrogenase/Acetyl-CoA synthase. *J. Am. Chem. Soc.* **1997**, *119*, 5648−5656.
(104) Panda, R.; Zhang, Y.; McLauchlan, C. C.; Rao, P. V.; Tiago de Oliveira, F. A.; Munck, E.; Holm, R. H. Initial structure modification of tetrahedral to planar nickel(II) in a nickel-iron-sulfur cluster related to the C-cluster of carbon monoxide dehydrogenase. *J. Am. Chem. Soc.* **2004**, *126*, 6448−6459.
(105) Sun, J.; Tessier, C.; Holm, R. H. Sulfur ligand substitution at the nickel(II) sites of cubane-type and cubanoid $NiFe_3S_4$ clusters relevant to the C-clusters of carbon monoxide dehydrogenase. *Inorg. Chem.* **2007**, *46*, 2691−2699.
(106) Majumdar, A. Bioinorganic modeling chemistry of carbon monoxide dehydrogenases: description of model complexes, current status and possible future scopes. *Dalton Trans.* **2014**, *43*, 12135−12145.
(107) Fesseler, J.; Jeoung, J. H.; Dobbek, H. How the $[NiFe_4S_4]$ cluster of CO dehydrogenase activates CO_2 and NCO^-. *Angew. Chem., Int. Ed.* **2015**, *54*, 8560−8564.
(108) Huang, D.; Holm, R. H. Reactions of the terminal Ni^{II}-OH group in substitution and electrophilic reactions with carbon dioxide and other substrates: structural definition of binding modes in an intramolecular $Ni^{II}\cdots Fe^{II}$ bridged site. *J. Am. Chem. Soc.* **2010**, *132*, 4693−4701.
(109) Prat, J. R.; Gaggioli, C. A.; Cammarota, R. C.; Bill, E.; Gagliardi, L.; Lu, C. C. Bioinspired nickel complexes supported by an iron metalloligand. *Inorg. Chem.* **2020**, *59*, 14251−14262.
(110) Ratliff, K. S.; Lentz, R. E.; Kubiak, C. P. Carbon dioxide chemistry of the trinuclear complex $[Ni_3(\mu_3\text{-CNMe})(\mu_3\text{-I})(dppm)_3][PF_6]$. Electrocatalytic reduction of carbon dioxide. *Organometallics* **1992**, *11*, 1986−1988.
(111) Agarwal, J.; Fujita, E.; Schaefer, H. F., III; Muckerman, J. T. Mechanisms for CO production from CO_2 using reduced rhenium tricarbonyl catalysts. *J. Am. Chem. Soc.* **2012**, *134*, 5180−5186.
(112) Pun, S.-N.; Chung, W.-H.; Lam, K.-M.; Guo, P.; Chan, P.-H.; Wong, K.-Y.; Che, C.-M.; Chen, T.-Y.; Peng, S.-M. Iron(I) complexes of 2,9-bis(2-hydroxyphenyl)-1,10-phenanthroline (H_2dophen) as electrocatalysts for carbon dioxide reduction. X-ray crystal structures of $[Fe(dophen)Cl]_2\cdot 2HCON(CH_3)_2$ and $[Fe(dophen)(N\text{-MeIm})_2]ClO_4$ (N-MeIm = 1-methylimidazole). *J. Chem. Soc., Dalton Trans.* **2002**, 575−583.
(113) Lam, F.; Feng, M.; Chan, K. S. Synthesis of dinucleating phenanthroline-based ligands. *Tetrahedron* **1999**, *55*, 8377−8384.
(114) Evans, D. F. The determination of the paramagnetic susceptibility of substances in solution by nuclear magnetic resonance. *J. Chem. Soc.* **1959**, *1959*, 2003−2005.
(115) Löliger, J.; Scheffold, R. Paramagnetic moment measurements by NMR. a micro technique. *J. Chem. Educ.* **1972**, *49*, 646−647.
(116) Juarez-Garcia, C.; Hendrich, M. P.; Holman, T. R.; Que, L.; Munck, E. Combined Möessbauer and EPR studies of the $S = 3$ state of an exchange-coupled $Fe^{III}Cu^{II}$ complex: test for quantitative EPR analysis of integer spin systems. *J. Am. Chem. Soc.* **1991**, *113*, 518−525.
(117) Hendrich, M. P.; Day, E. P.; Wang, C.-P.; Synder, B. S.; Holm, R. H.; Münck, E. Ground-state electronic structures of binuclear iron(II) sites: experimental protocol and a consistent description of Möessbauer, EPR, and magnetization measurements of the bis-(phenolate)-bridged complex $[Fe_2(salmp)_2]^{2-}$. *Inorg. Chem.* **1994**, *33*, 2848−2856.
(118) Reger, D. L.; Pascui, A. E.; Smith, M. D.; Jezierska, J.; Ozarowski, A. Dinuclear complexes containing linear M−F−M [M = Mn(II), Fe(II), Co(II), Ni(II), Cu(II), Zn(II), Cd(II)] bridges: trends in structures, antiferromagnetic superexchange interactions, and spectroscopic properties. *Inorg. Chem.* **2012**, *51*, 11820−11836.
(119) The structure and overall charge of $Zn_3(bphpp)(AcO)_4$ are different from those of **NiNi(bphpp)**. The CV comparison of $Zn_3(bphpp)(AcO)_4$ and **NiNi(bphpp)** is only intended to be utilized to assign the reduction processes of the phenanthroline unit.
(120) Nichols, A. W.; Chatterjee, S.; Sabat, M.; Machan, C. W. Electrocatalytic reduction of CO_2 to formate by an iron schiff base complex. *Inorg. Chem.* **2018**, *57*, 2111−2121.
(121) Appel, A. M.; Helm, M. L. Determining the overpotential for a molecular electrocatalyst. *ACS Catal.* **2014**, *4*, 630−633.
(122) Machan, C. W.; Chabolla, S. A.; Kubiak, C. P. Reductive Disproportionation of Carbon Dioxide by an Alkyl-Functionalized Pyridine Monoimine Re(I) fac-Tricarbonyl Electrocatalyst. *Organometallics* **2015**, *34*, 4678−4683.
(123) Sampson, M. D.; Kubiak, C. P. Manganese electrocatalysts with bulky bipyridine ligands: utilizing Lewis acids to promote carbon dioxide reduction at low overpotentials. *J. Am. Chem. Soc.* **2016**, *138*, 1386−1393.
(124) Costentin, C.; Drouet, S.; Robert, M.; Savéant, J.-M. Turnover numbers, turnover frequencies, and overpotential in molecular catalysis of electrochemical reactions. Cyclic voltammetry and preparative-scale electrolysis. *J. Am. Chem. Soc.* **2012**, *134*, 11235−11242.
(125) Costentin, C.; Savéant, J.-M. Multielectron, multistep molecular catalysis of electrochemical reactions: benchmarking of homogeneous catalysts. *ChemElectroChem.* **2014**, *1*, 1226−1236.
(126) Wang, V. C.-C.; Johnson, B. A. Interpreting the electrocatalytic voltammetry of homogeneous catalysts by the foot of the wave analysis and its wider implications. *ACS Catal.* **2019**, *9*, 7109−7123.
(127) Since the electrocatalytic CO_2 reduction disproportionation at corresponding reduction peak is an electrochemical-multi-chemical process, the TOF_{calc} is the rate of the chemical rate-determining step (C-O activation step of **NiNi(bphpp)** and C-O cleavage step of **Ni(hbpp)**) following the reduction but not the TOF_{max}.
(128) Lu, T.; Chen, F. Multiwfn: a multifunctional wavefunction analyzer. *J. Comput. Chem.* **2012**, *33*, 580−592.
(129) Humphrey, W.; Dalke, A.; Schulten, K. VMD: visual molecular dynamics. *J. Mol. Graph.* **1996**, *14*, 33−38.
(130) Yoo, C.; Lee, Y. Carbon dioxide binding at a Ni/Fe center: synthesis and characterization of $Ni(\eta^1\text{-}CO_2\text{-}\kappa C)$ and $Ni\text{-}\mu\text{-}CO_2\text{-}\kappa C\text{:}\kappa^2 O$. *O′-Fe. Chem. Sci.* **2017**, *8*, 600−605.

https://doi.org/10.1021/jacsau.4c00047
JACS Au 2024, 4, 1207−1218

(131) Oren, D.; Diskin-Posner, Y.; Avram, L.; Feller, M.; Milstein, D. Metal-ligand cooperation as key in formation of dearomatized Ni^{II}-H pincer complexes and in their reactivity toward CO and CO_2. *Organometallics* **2018**, *37*, 2217−2221.
(132) Kozuch, S.; Shaik, S. How to conceptualize catalytic cycles? The energetic span model. *Acc. Chem. Res.* **2011**, *44*, 101−110.
(133) Garay-Ruiz, D.; Bo, C. Revisiting catalytic cycles: a broader view through the energy span model. *ACS Catal.* **2020**, *10*, 12627−12635.
(134) Su, X. J.; Gao, M.; Jiao, L.; Liao, R.-Z.; Siegbahn, P. E. M.; Cheng, J.-P.; Zhang, M.-T. Electrocatalytic water oxidation by a dinuclear copper complex in a neutral aqueous solution. *Angew. Chem., Int. Ed.* **2015**, *54*, 4909−4914.
(135) Du, H.-Y.; Chen, S.-C.; Su, X.-J.; Jiao, L.; Zhang, M.-T. Redox-active ligand assisted multielectron catalysis: a case of Co^{III} Complex as water oxidation catalyst. *J. Am. Chem. Soc.* **2018**, *140*, 1557−1565.
(136) Shi, J.; Guo, Y.-H.; Xie, F.; Chen, Q.-F.; Zhang, M.-T. Redox-active ligand assisted catalytic water oxidation by a Ru^{IV}=O intermediate. *Angew. Chem., Int. Ed.* **2020**, *59*, 4000−4008.
(137) Zhang, H.-T.; Su, X.-J.; Xie, F.; Liao, R.-Z.; Zhang, M.-T. Iron-catalyzed water oxidation: O-O bond formation via intramolecular oxo-oxo interaction. *Angew. Chem., Int. Ed.* **2021**, *60*, 12467−12474.
(138) Chen, Q.-F.; Xiao, Y.; Liao, R.-Z.; Zhang, M.-T. Trinuclear nickel catalyst for water oxidation: intramolecular proton-coupled electron transfer triggered trimetallic cooperative O−O bond formation. *CCS Chem.* **2022**, *5*, 245−256.
(139) Zhang, H.-T.; Guo, Y.-H.; Xiao, Y.; Du, H.-Y.; Zhang, M.-T. Heterobimetallic NiFe cooperative molecular water oxidation catalyst. *Angew. Chem., Int. Ed.* **2023**, *62*, No. e202218859.
(140) Shi, J.; Guo, Y.-H.; Xie, F.; Zhang, M.-T.; Zhang, H.-T. Electronic effects of redox-active ligands on ruthenium-catalyzed water oxidation. *Chin. J. Catal.* **2023**, *52*, 271−279.
(141) Chen, Q.-F.; Xian, K.-L.; Zhang, H.-T.; Su, X.-J.; Liao, R.-Z.; Zhang, M.-T. Pivotal role of geometry regulation on O−O bond formation mechanism of bimetallic water oxidation catalysts. *Angew. Chem., Int. Ed.* **2024**, *63*, No. e202317514.

https://doi.org/10.1021/jacsau.4c00047
JACS Au 2024, 4, 1207−1218